Learning-dependent cholinergic plasticity reconfigures cortical circuit dynamics.

Authors: Andrew H. Moberly[1], Jessica A. Cardin[1,2], Michael J. Higley[1,2,3]

Affiliation: [1] Dept. of Neuroscience
[2] Dept. of Psychiatry
[3] Dept. of Biomedical Engineering
Yale University, New Haven, CT

Correspondence: Jessica A. Cardin or Michael J. Higley
jess.cardin@yale.edu
m.higley@yale.edu

Referenced Summary Paragraph (<200 words)

Neuromodulation by acetylcholine (ACh) plays a critical role in reshaping neural dynamics in the neocortex as a function of development, behavioral state, and learning [1-6]. Prior work suggests cholinergic signaling can act as a gate for the subsequent induction of circuit plasticity [3,7,8]. However, modification of ACh release could also be a direct mechanism for the expression of cortical plasticity. Here, we combine widefield and 2-photon imaging in head-fixed mice to show that visual fear conditioning leads to a selective, cue-dependent release of ACh in primary visual cortex that enhances visually-evoked neuronal responses via excitation of layer 1 GABAergic interneurons and resulting disinhibition of local excitatory pyramidal neurons. Cholinergic signaling through muscarinic receptors in visual cortex is necessary for both the enhanced visual response and conditioned fear behavior. Our results demonstrate a novel capacity for conditioned release of ACh in sensory cortex to serve as a mechanism for sensory-guided behavioral learning. Rather than acting as a simple gate, cortical neuromodulation may thus play a central role in the expression of learned behavior.

Main Text

Release of neuromodulators such as acetylcholine (ACh) is coupled to spontaneous variation in behavioral state and dynamically reconfigures local and long-range circuit organization across the neocortex [4,9,10]. Cholinergic release also occurs following delivery of rewarding and aversive stimuli, potentially playing a role in learning-dependent plasticity in cortical networks [2,4,9-16]. A rich literature demonstrates that learning to associate sensory cues with reinforcement or punishment modifies neural representations of behavioral task variables and alters the sensitivity of responses to subsequent external inputs [17-24]. This network-level plasticity may reflect the reorganization of local microcircuits, including subpopulations of GABAergic interneurons, many of which express cholinergic receptors [25-27]. Indeed, cholinergic modulation of cortical inhibition is implicated in state-dependent cortical activity [11,25,28,29]. However, the potential for direct learning-related plasticity of cortical ACh release in sensory areas and the consequences for circuit dynamics and behavior remain unexplored.

Classical fear conditioning involves repeated pairing of a neutral sensory cue with an aversive stimulus such as a mild foot-shock [30,31]. In primary auditory cortex, fear conditioning can enhance sensory-evoked activity of layer 2/3 excitatory pyramidal neurons (PNs) and shift their tuning properties towards the conditioned frequency [32-34], a form of plasticity that requires activation of muscarinic ACh receptors [5,6,8,35,36]. Indeed, foot-shock drives acute ACh release in auditory cortex of untrained anesthetized animals, potentially disinhibiting PNs via activation of layer 1 GABAergic interneurons (L1-INs) that in turn suppress layer 2/3 parvalbumin-expressing interneurons (PV-INs) [3]. This acute disinhibition is thought to gate the induction of learning-dependent cortical plasticity [37-40]. However, the dynamics and plasticity of ACh release during task learning and their role in the expression of learned behavior are unknown.

To investigate how learning modifies both ACh release and the functional organization of cortical microcircuits, we developed a novel visually-cued fear conditioning task in which head-fixed mice learn to associate a brief visual stimulus with a mild foot-shock (Figure 1a). Animals were first water-deprived, acclimated to head-fixation, and trained to lick a spout for freely available water. We then presented a visual stimulus comprising a 5s full-screen, dynamic filtered noise pattern for 10-20 trials per day with a random intertrial interval (ITI, see Methods). Animals were shown the visual stimulus alone for three days to assess baseline licking behavior. Beginning on the fourth day, the visual stimulus was followed after a 1s gap by a mild foot-shock that resulted in immediate cessation of licking behavior. Repeated stimulus-shock pairings rapidly induced learned lick suppression at the onset of the visual cue that lasted for the duration of the stimulus presentation and persisted for several seconds (Extended Data Figure 1). We quantified licking behavior using a lick rate index calculated over the 5s visual stimulus duration $(Rate_{Post}-Rate_{Pre})/(Rate_{Post}+Rate_{Pre})$. This value decreased immediately on the first day of conditioning and reached a plateau within 2-3 days (Figure 1b). Overall, there was a significant reduction in lick index for the population (Pre vs. Post, -0.11±0.04 vs. -0.76±0.12, $p<0.01$ Paired t-test, n=17 mice, Figure 1c).

Conditioning did not significantly change the baseline lick rate during the ITI (Extended Data Figure 1). Moreover, conditioning did not alter basal arousal level associated with head-fixation or placement in the experimental setup, as indicated by the lack of difference in the average ITI pupil size before and after stimulus-

shock pairing. However, conditioning did produce a significant increase in pupil dilation associated with the onset of the visual stimulus (Extended Data Figure 1). Similar levels of learned lick suppression were observed across multiple independent cohorts of mice used throughout the present study (Extended Data Figure 1), demonstrating the reproducibility of this assay for quantifying visually cued conditioning.

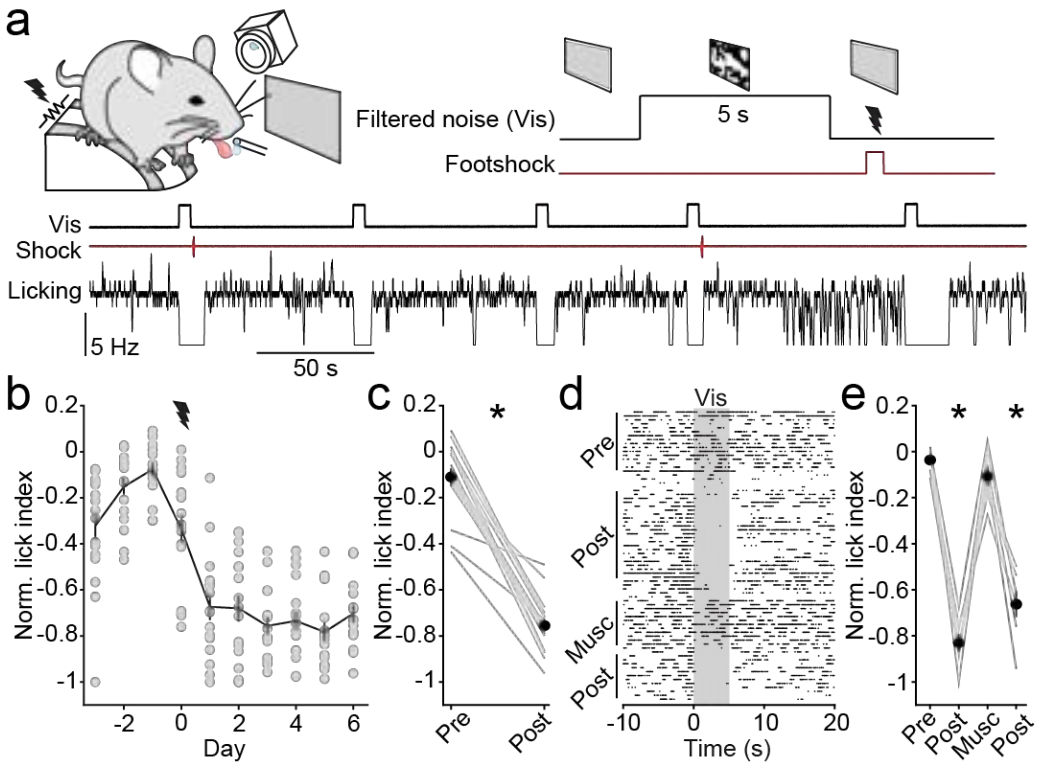

Figure 1: **Visually-cued lick suppression is rapidly induced and dependent on visual cortex activity**. (**a**) Schematic of the behavioral setup. During conditioning, a 5-second filtered noise stimulus is followed by a 1-second trace and a 0.5-second foot-shock. Below are example traces of the visual stimulus presentation, foot-shock, and lick-rate from a portion of a post-conditioning session. (**b**) Normalized lick indices per day, with day 0 as the first session where the conditioned stimulus was paired with foot-shock (n=17 mice). (**c**) Average pre- and post-conditioning lick indices (n=17 mice, session averages from each mouse are shown in gray) * indicates $p<0.05$, paired t-test. (**d**) Example lick raster aligned to visual stimulus onset (gray bar) across pre- and post-conditioning, muscimol session (musc), and post-muscimol session. (**e**) Average pre, post conditioning, muscimol session, and post muscimol session conditioning lick indices (n=7 mice) * indicates $p<0.05$ for pairwise post-hoc comparisons (Tukey-Kramer corrected) against pre-conditioning session following a significant ($p<0.05$) main effect of session in repeated measures ANOVA. For panels **b**,**c**, & **e**, data are represented as mean ± SEM.

Normal activity in primary visual cortex (VisP) was necessary for the expression of learning, as acute intracortical injection of the GABA receptor agonist muscimol reversibly abolished conditioned lick suppression ($p<0.01$ ANOVA, $p<0.01$ Tukey's Post-hoc for muscimol vs. control, n=7 mice, Figure 1d-e) with no change in basal lick rate during the ITI (Extended Data Figure 1). Moreover, conditioned behavior was sensitive to the contrast of the visual stimulus (Extended Data Figure 1). Head-fixed mice can thus readily form a robust, cortex-dependent association between a previously neutral visual cue and an aversive unconditioned stimulus.

To explore how this form of learning impacts the cortical representation of the visual cue, we first assessed cortical activity using widefield, mesoscopic calcium imaging [4,41,42]. We used neonatal injections of

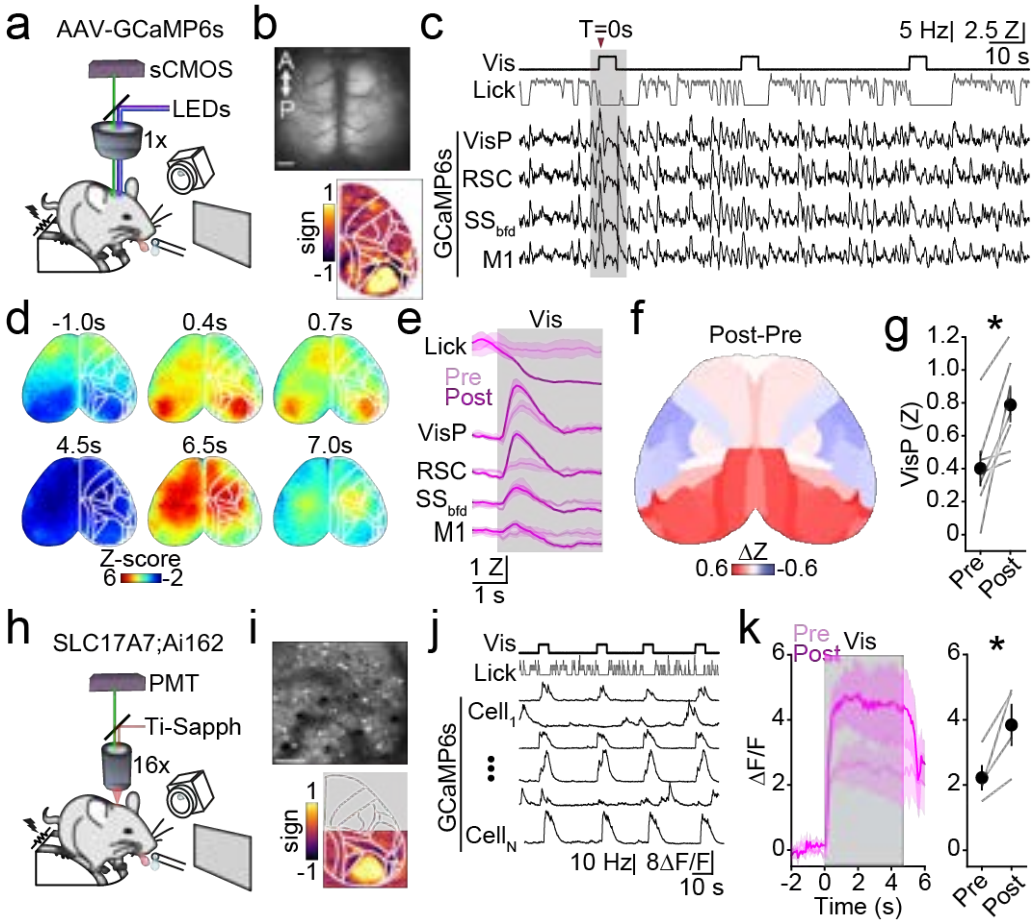

Figure 2: Visual fear-conditioning enhances visually-evoked activity. (**a**) Schematic of the widefield imaging setup. (**b**) Top: example transcranial imaging field of view showing GCaMP6s expression. Scale bar: 1mm. Bottom: averaged retinotopic field sign maps with Allen CCFv3 parcels overlaid in white. (**c**) Example time series from a portion of a post-conditioning session showing onsets of visual stimuli, lick-rate, and traces corresponding to calcium activity in Allen parcels (VisP; primary visual cortex, RSC; retrosplenial cortex, SS_{bfd}; somatosensory cortex barrel field, M1; primary motor cortex). (**d**) Example image frames showing the visual stimulus response post-conditioning from the gray segment in (**c**). Times in seconds are relative to visual stimulus onset at t=0s (indicated in (**c**) by the red arrowhead). White lines indicate Allen CCFv3-derived parcellation. (**e**) Traces show visual stimulus-averaged activity pre- and post-conditioning from the Allen parcels in (**c**) (n=7 mice). (**f**) Average spatial map of the difference (post minus pre-conditioning) in the visual response amplitude for each Allen parcel (n=7 mice). (**g**) Average response in VisP parcel pre- and post-conditioning (n=7 mice). * indicates $p<0.05$, paired t-test. (**h**) Schematic of the 2-photon imaging setup. (**i**) Top: example 2-photon imaging field of view. Scale bar, 100 µm. Bottom: averaged retinotopic field sign maps with Allen CCFv3 parcels overlaid in white. (**j**) Example time series from one animal from a portion of a post-conditioning session showing onsets of visual stimuli, lick-rate, and traces corresponding to selected cell regions of interest. (**k**) Left: Averaged stimulus-aligned visual response pre- and post-conditioning in excitatory cells. Right: Average response amplitude pre- and post-conditioning (n=4 mice). * indicates $p<0.05$, paired t-test. For panels **e**,**g**, & **k**, data are represented as mean ± SEM.

adeno-associated virus (AAV) into the cerebral vasculature to induce cortex-wide expression of the green fluorescent calcium indicator GCaMP6s [4,43-45]. Adult mice were then trained as described above while under the microscope objective (Figure 2a). Mesoscopic imaging through the intact skull generated robust signals across the dorsal neocortex, sufficient for monitoring both spontaneous and visually evoked activity (Figure 2b-c). We

used a series of drifting filtered-noise bars (see Methods) to map the retinotopic borders of VisP and higher-order visual areas based on fluorescent calcium signaling (Figure 2b), allowing us to quantify neural activity from identified regions during task performance. Individual trials showed a characteristic visually-evoked response that began in VisP and rapidly spread throughout much of the cortex, as in previous work [46], followed by a large foot-shock-evoked response (Figure 2c-d).

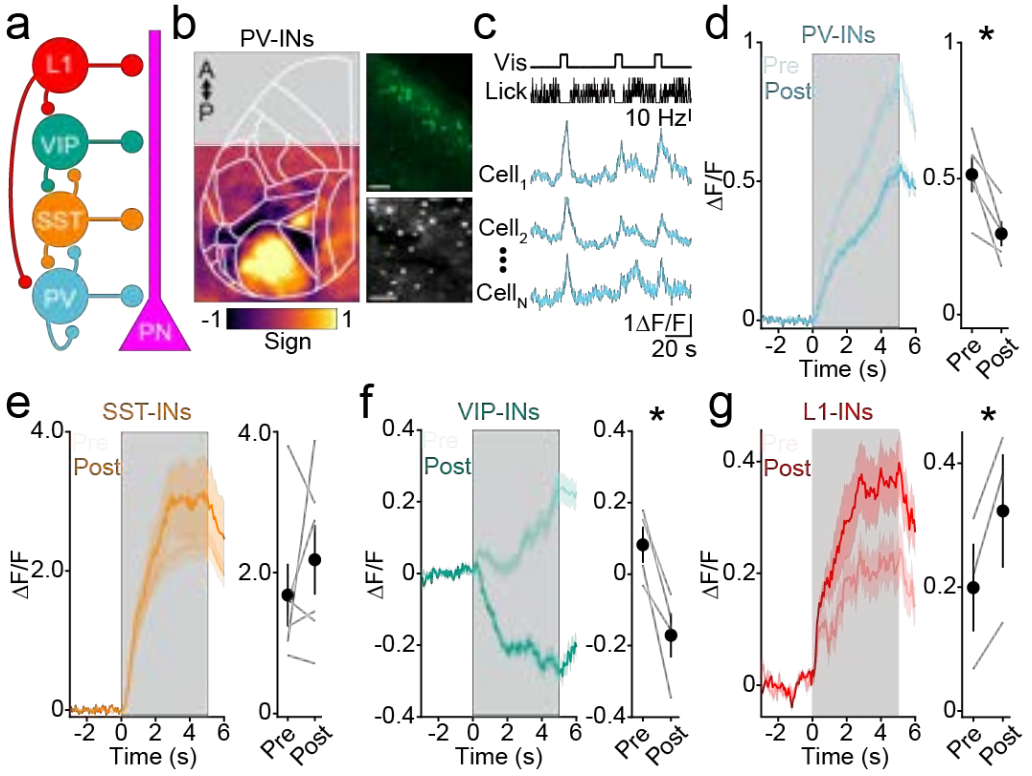

Figure 3: GABAergic plasticity following visual fear conditioning. (**a**) Schematic of local cortical circuitry. (**b**) Left: averaged retinotopic field sign map in GCaMP6s expressing PV-Cre mice (n=5 mice). Right: confocal image of GCaMP6s-expressing PV-INs in layer 2/3 in an example PV-Cre mouse. Scale bar, 70 μm. Below is an example 2-photon field of view. Scale bar, 50 μm. (**c**) Example time series from one animal from a segment of a post-conditioning session showing onsets of visual stimuli, lick-rate, and traces corresponding to selected cell regions of interest. (**d**) Left: Averaged stimulus-aligned visual response pre- and post-conditioning in PV-INs. Gray box indicates the time of the visual stimulus. Right: Average response amplitude during the visual response (n=5 mice). (**e-g**) Same as in (**d**) for SST-INs, VIP-INs and L1-INs (n=6 SST-Cre mice; n=4 VIP-Cre mice; n=3 mDLX-GCaMP6f L1 mice). * indicates p<0.05, paired t-test. For panels **d**,**e**,**f**,**g**, data are represented as mean ± SEM.

Imaged mice exhibited robust learning-induced lick suppression (Extended Data Figure 1), and we compared visually-evoked signals before and after conditioning, finding a ~2-fold increase in the magnitude of the visual response that was greatest in posterior cortical regions (Figure 2e-f, Extended Data Figure 2). The evoked response in VisP increased significantly with learning (Pre vs. Post, 0.40±0.11 Z vs. 0.79±0.11 Z, p=0.013, paired t-test, n=7 mice, Figure 2g). Averaging cortical signals around spontaneous periods of lick cessation during the ITI showed no change in VisP activity and a modest reduction in activity within frontal motor areas (Extended Data Figure 2), suggesting that the change in visual response was not related to motor behavior. In a separate cohort of animals, we found that the conditioning-associated increase in visual response was

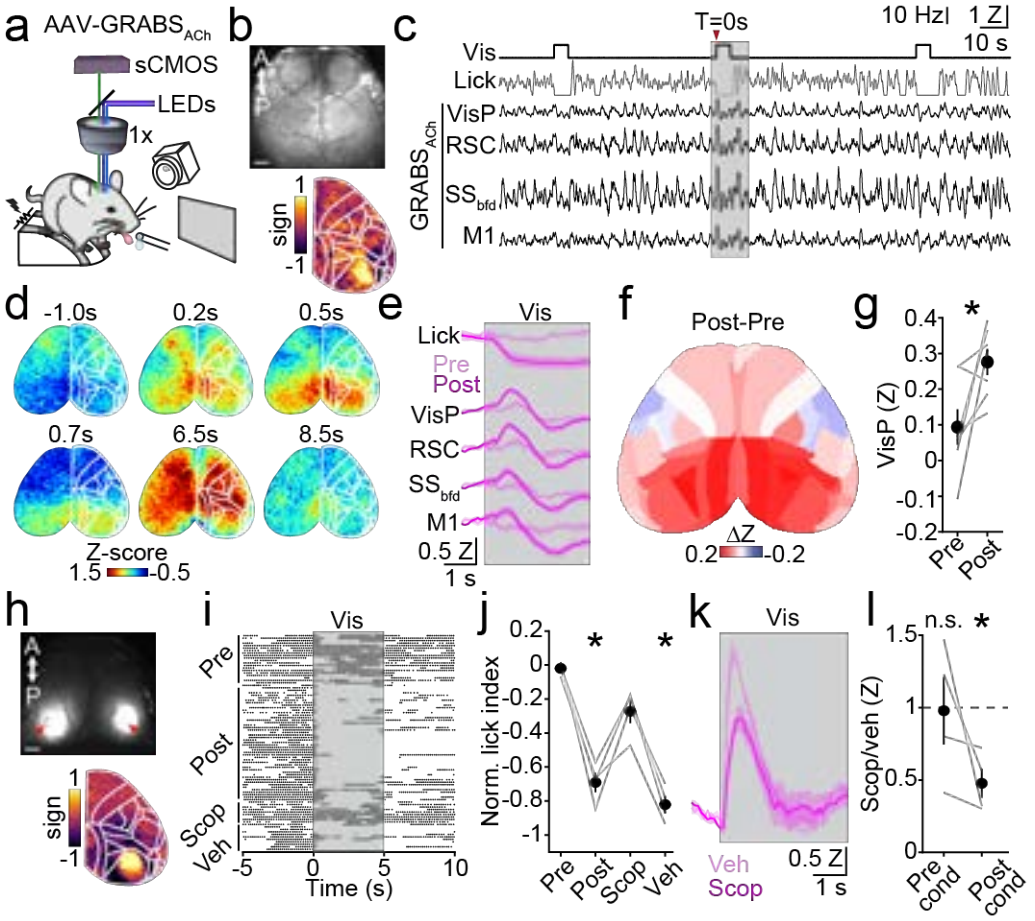

Figure 4: Cholinergic plasticity following visual fear conditioning. (**a**) Schematic of the widefield imaging setup. (**b**) Top: Example transcranial imaging field of view showing GRABS$_{ACh}$ expression. Scale bar: 1mm. Bottom: Averaged, intrinsic-imaging derived, retinotopic field sign maps with Allen CCFv3 parcels overlaid in white. (**c**) Example time series from one animal from a segment of a post-conditioning session showing onsets of visual stimuli, lick-rate, and traces corresponding to GRABS$_{ACh}$ activity in Allen parcels (VisP; primary visual cortex, RSC; retrosplenial cortex, SS$_{bfd}$; somatosensory cortex barrel field, M1; primary motor cortex). (**d**) Example image frames showing the visual stimulus response post-conditioning from the gray segment in (**c**). Times in seconds are relative to visual stimulus onset at t=0s (indicated in (**c**) by the red arrowhead). White lines indicate Allen CCFv3-derived parcellation. (**e**) Traces show visual stimulus-averaged activity pre- and post-conditioning (n=7 mice) from the Allen parcels in (**c**). (**f**) Average spatial map of the difference (post-preconditioning) in the visual response for each Allen parcel (n=7 mice). (**g**) Average GRABS$_{Ach}$ response in VisP parcel pre- and post-conditioning (n=7 mice). * indicates $p<0.05$, paired t-test. (**h**) Top: example transcranial imaging field of view showing GCaMP8m expression three weeks after AAV injection. Red arrowheads indicate locations of craniotomies for local pharmacology experiments. Scale bar: 1mm. Bottom: averaged retinotopic field sign maps with Allen CCFv3 parcels overlaid in white. (**i**) Example lick raster aligned to visual stimulus onset (gray bar) across pre- and post-conditioning, a scopolamine session (scop), and a post-scopolamine, vehicle session. (**j**) Average pre-, post-conditioning, scopolamine session, and vehicle session conditioning lick indices (n=4 mice). * indicates $p<0.05$ for pairwise post-hoc comparisons (Tukey-Kramer corrected) against pre-conditioning session following a significant ($p<0.05$) main effect of session in repeated measures ANOVA. (**k**) Traces show visual stimulus-averaged activity post-conditioning from visual cortex after local injection of either scopolamine or vehicle (n=4 mice). (**l**) Magnitude of visual response (Scopolamine/vehicle) pre- and post-conditioning. * indicates $p<0.05$ for one-sample t-test comparing population response to hypothesized mean of 1. For **e**,**g**,**j**,**k**, & **l** data are represented as mean ± SEM.

specific to the stimulus paired with foot-shock. Mice trained on a task variant with a CS+ and CS- paired and unpaired with shock, respectively, readily demonstrated lick suppression only to the CS+ (Extended Data Figure 2). Moreover, training significantly enhanced the VisP response to the CS+ over the CS- (Extended Data Figure 2). Thus, visually cued fear conditioning results in a selective enhancement of the cortical response to the conditioned stimulus.

Mesoscopic imaging data reflect spatially averaged signals arising from cell bodies and the surrounding neuropil [43,47-50]. Therefore, to determine whether learning produces a specific increase in the activity of individual VisP neurons, we carried out 2-photon calcium imaging in a separate cohort of transgenic mice conditionally expressing GCaMP6s in excitatory VGlut1-expressing PNs [51] (Figure 2h). Mice were implanted with a titanium headpost and glass cranial window over VisP and behaviorally conditioned as described above. For each mouse, we initially used mesoscopic imaging to identify the borders of VisP, followed by 2-photon imaging of individual layer 2/3 PNs (L2/3 PNs) (Figure 2i). Again, training produced significant lick suppression across the group (Figure. 2j). Consistent with our mesoscopic data, conditioning was associated with a significant increase in the magnitude of the visually-evoked response for individual L2/3 PNs (Pre vs. Post, 2.2±3.8 ΔF/F vs. 3.8±0.6 ΔF/F, p=0.04, paired t-test, n=4 mice, Figure 2k, Extended Data Figure 3). Taken together, our mesoscopic and 2-photon imaging results indicate that visual fear-conditioning induces a significant, stimulus-specific enhancement of PN sensory representation in VisP.

Visually-evoked activity in the neocortex is strongly shaped by the interplay between excitatory PNs and diverse subpopulations of GABAergic INs [52] (Figure 3a). In particular, PV-INs play a well-established role in constraining the magnitude and timing of PNs output [53-56]. We tested the hypothesis that enhanced visual responses might be associated with a weakening of PV-IN activity following learning. We expressed GCaMP6s in PV-INs of VisP via local AAV injection (see Methods) and carried out 2-photon imaging of these cells during conditioning (Figure 3b-c). As above, these mice readily learned to associate the visual cue with shock (Extended Data Figure 1). However, in contrast to results from PN imaging, conditioning induced a significant reduction in the magnitude of visual responses in PV-INs (Pre vs. Post, 0.51±0.06 ΔF/F vs. 0.30±0.05 ΔF/F, p=0.02, paired t-test, n=5 mice, Figure 3d, Extended Data Figure 3).

In addition to PV-INs, GABAergic interneurons expressing either somatostatin- (SST-INs) or vasoactive intestinal peptide (VIP-INs) play key roles in shaping the activity of PNs in VisP [28,57-61] (Figure 3a). Therefore, we used a similar strategy to image the visually evoked responses in these cell types before and after conditioning. Mice expressing GCaMP6f in either SST-INs or VIP-INs reliably exhibited conditioned lick suppression (Extended Data Figure 1). While SST-INs did not show a significant change in visual response associated with training (Pre vs. Post, 1.68±0.44 ΔF/F vs. 2.18±0.49 ΔF/F, p=0.40, paired t-test, n=6 mice, Figure 3e, Extended Data Figure 3), VIP-IN responses were significantly reduced below baseline levels (Pre vs. Post, 0.08±0.05 ΔF/F vs. -0.17±0.06 ΔF/F, p=0.018, paired t-test, n=4 mice, Figure 3f, Extended Data Figure 3). Fear conditioning thus selectively induces a broad suppression of sensory-evoked GABAergic output in two major classes of VisP interneurons.

Recent studies have suggested that GABAergic interneurons residing in Layer 1 can provide blanket inhibition to multiple postsynaptic interneuron classes [37,62-66] (Figure 3a). We reasoned that these cells might be well-positioned to enhance visual responses in PNs via disinhibition of local GABAergic microcircuits. To explore this hypothesis, we expressed GCaMP6s in VisP via AAV with an interneuron-specific enhancer [67] and carried out 2-photon imaging of cell bodies in layer 1 (Extended Data Figure 3). Again, these mice readily learned the task (Extended Data Figure 1). In contrast to the other interneuron subpopulations, conditioning produced a significant increase in the magnitude of the L1-IN visually evoked response (Pre vs. Post, 0.20±0.07 ΔF/F vs. 0.32±0.09 ΔF/F, p=0.04, paired t-test, n=3 mice, Figure 3g, Extended Data Figure 3). Combined with our other imaging data, these results suggest that visual fear conditioning induces a significant enhancement of sensory-evoked activity in L1-INs, leading to a suppression of activity in both PV- and VIP-INs and a disinhibitory increase in PN output.

Cholinergic modulation is strongly implicated in behavioral state- and learning-dependent variation in cortical circuit dynamics [6,9,68-72]. We therefore hypothesized that plasticity of cortical ACh release might underlie the functional reorganization of visual representation. To explore this possibility, we used neonatal AAV injection to drive pan-cortical expression of the green fluorescent ACh sensor $GRABS_{ACh}$ [4,73] and used mesoscopic imaging to monitor cholinergic dynamics before and after conditioning (Figure 4a). Hemodynamic imaging, paired with the presentation of drifting filtered-noise bars, allowed us to identify VisP in these animals (Figure 3b). Imaging in naïve mice revealed spatiotemporally dynamic and heterogeneous spontaneous ACh release across the cortex and a weak signal in visual areas associated with stimulus onset (Figure 4c-e). However, after training, presentation of the visual cue elicited a robust ACh release that was selective for posterior "visual" versus anterior "motor" cortical areas (Figure 4d-f, Extended Data Figure 4). Within VisP, the evoked $GRABS_{ACh}$ signal was significantly different before and after learning (Pre vs. Post, 0.09±0.05 Z vs. 0.27±0.04 Z, p=0.033, paired t-test, n=7 mice, Figure 4g, Extended Data Figure 4). As with the training-induced enhancement of neural activity, this increased ACh release was not due to reduced motor activity per se, as spontaneous lick pauses did not produce measurable ACh signals (Extended Data Figure 4). Fear conditioning thus induces a significant, spatially restricted increase in ACh release evoked by the conditioned visual cue, indicating learning-dependent plasticity of ACh dynamics in the cortex.

Finally, we examined whether these cholinergic dynamics were necessary for both the expression of conditioned behavior and the enhancement of the cortical visual representation. For these experiments, we locally expressed GCaMP8s bilaterally in VisP using intracortical AAV injection and targeted craniotomies to VisP for local bilateral drug infusion. This approach again allowed us to monitor cortical activity, including retinotopic identification of VisP borders (Figure 4h). After behavioral training, we infused the muscarinic antagonist scopolamine into both hemispheres, finding that blocking cholinergic signaling significantly disrupted conditioned lick behavior ($p<0.01$ Repeated measures ANOVA, $p<0.01$ Tukey's post-hoc test for scopolamine versus vehicle, n=4 mice, Figure 4j). We also quantified the effect of scopolamine on visually-evoked activity in VisP. Prior to conditioning, intracortical muscarinic blockade had no significant impact on the magnitude of the sensory response (Ratio of response with scopolamine to that with vehicle vs. 1.0, 0.98±0.23, p=0.93, t-test, n=4

mice). However, after learning, intra-VisP scopolamine significantly reduced the visually-evoked response magnitude (Ratio of response with scopolamine to that with vehicle vs. 1.0, 0.48±0.10, p=0.014, t-test, n=4 mice). Enhanced cholinergic signaling via muscarinic receptors in VisP is therefore necessary for both conditioned behavior and the learning-dependent increase in cortical visual representation.

Cholinergic modulation exerts profound control over neural circuits throughout the brain, including the neocortex [74,75]. Fluctuations in cortical ACh release are strongly linked to variation in behavioral state, including changes in arousal and attention [4,9,10,76]. Additionally, delivery of unexpected rewarding or aversive stimuli are associated with cortical release of ACh [2,13,14,16,77]. Moreover, presentation of sensory cues associated with reward or punishment can induce firing of cholinergic basal forebrain neurons [2,78,79] and drive release of ACh within the prefrontal cortex [16,80-82]. However, work in somatosensory and auditory cortex has suggested that cholinergic signals may be coupled to conditioned motor behaviors rather than sensory cues [77]. Functionally, ACh release can modulate neuronal excitability and synaptic transmission, shaping firing rates and patterned network activity [11,83,84]. In addition, behaviorally-coupled ACh release is hypothesized to play a critical role in gating learning-related plasticity in cortical circuits. For example, electrical stimulation of the basal forebrain induces shifts in the receptive field structure of neurons in auditory cortex [2,7,8]. In these studies, ACh was considered to gate subsequent plasticity in cortical circuits, potentially through a temporary relief of GABAergic inhibition that enabled momentary release of firing in auditory cortex [3]. Moreover, the acquisition of reward timing by visual cortex neurons was shown to require ACh release for the induction of plasticity but was unnecessary for the expression of the learned firing patterns [12]. In contrast, we observed that visual fear conditioning resulted in sensory-evoked ACh release within VisP that was necessary for both learned behavior and learning-associated enhancement of sensory representation. Thus, we find that learning-induced plasticity of ACh release can serve as the primary mechanism of expression for conditioned behavior.

Our observation that visual fear conditioning resulted in a spatially restricted, sensory-induced release of ACh in posterior cortical areas is consistent with earlier work from our lab showing that spontaneous fluctuations in behavioral state are associated with dynamic, spatiotemporally heterogeneous activity [4]. Moreover, anatomical studies show that distinct populations of cholinergic neurons in the basal forebrain exhibit diverse long-range projection patterns [85-88], and recent work demonstrates ACh release in visual areas may exhibit retinotopy [89]. Our results suggest that learning is associated with plasticity in the cholinergic system, promoting visually-induced ACh release selectively in visual areas and contributing to heterogeneous modulation across the cortex. The mechanisms of this plasticity remain unknown, but may reflect circuit coordination between visual and frontal cortex and the basal forebrain and the potential for modification of descending control over cholinergic neuronal activity.

In line with our findings, prior studies also found that learning reconfigures the functional organization of cortical GABAergic circuits in both auditory and visual areas [90-92]. However, the mechanisms driving learning-dependent changes in interneuron dynamics have been largely unexplored. Our results suggest sensory-evoked ACh release as a candidate explanation, in which cholinergic excitation of L1-INs [29,93] drives inhibition of VIP- and PV-INs and subsequent disinhibition of PN output. L1-INs, and particularly those expressing NDNF, have

emerged as a potential state-dependent controller of local cortical circuits [37,62,63,65,94] that may be critical for both induction and expression of learning [3,37,39,65]. We propose that learning-dependent plasticity of ACh release harnesses this circuit motif to promote conditioned, visually-guided behavior. Notably, VIP-mediated circuit disinhibition has also been posited as a key motif in cortical circuits [59-61]. However, our results suggest that, under circumstances of behaviorally-cued ACh release, L1-IN-mediated inhibition of VIP-INs dominates the direct cholinergic excitation of the latter population.

In conclusion, we demonstrate that visually cued fear conditioning results in selective, sensory-evoked ACh release in VisP enhancing sensory representations and promoting visually guided behavior by engaging a disinhibitory GABAergic circuit motif. Thus, plasticity of cholinergic release and dynamic circuit reconfiguration may be a broad mechanism for learning-dependent modification of cortical circuits necessary for behavior.

References

1 Butt, A. E. *et al.* Association learning-dependent increases in acetylcholine release in the rat auditory cortex during auditory classical conditioning. *Neurobiol Learn Mem* **92**, 400-409, doi:10.1016/j.nlm.2009.05.006 (2009).

2 Guo, W., Robert, B. & Polley, D. B. The Cholinergic Basal Forebrain Links Auditory Stimuli with Delayed Reinforcement to Support Learning. *Neuron* **103**, 1164-1177 e1166, doi:10.1016/j.neuron.2019.06.024 (2019).

3 Letzkus, J. J. *et al.* A disinhibitory microcircuit for associative fear learning in the auditory cortex. *Nature* **480**, 331-335, doi:10.1038/nature10674 (2011).

4 Lohani, S. *et al.* Spatiotemporally heterogeneous coordination of cholinergic and neocortical activity. *Nat Neurosci* **25**, 1706-1713, doi:10.1038/s41593-022-01202-6 (2022).

5 Miasnikov, A. A., McLin, D., 3rd & Weinberger, N. M. Muscarinic dependence of nucleus basalis induced conditioned receptive field plasticity. *Neuroreport* **12**, 1537-1542, doi:10.1097/00001756-200105250-00047 (2001).

6 Tinsley, M. R., Quinn, J. J. & Fanselow, M. S. The role of muscarinic and nicotinic cholinergic neurotransmission in aversive conditioning: comparing pavlovian fear conditioning and inhibitory avoidance. *Learn Mem* **11**, 35-42, doi:10.1101/lm.70204 (2004).

7 Froemke, R. C. *et al.* Long-term modification of cortical synapses improves sensory perception. *Nat Neurosci* **16**, 79-88, doi:10.1038/nn.3274 (2013).

8 Froemke, R. C., Merzenich, M. M. & Schreiner, C. E. A synaptic memory trace for cortical receptive field plasticity. *Nature* **450**, 425-429, doi:10.1038/nature06289 (2007).

9 Collins, L., Francis, J., Emanuel, B. & McCormick, D. A. Cholinergic and noradrenergic axonal activity contains a behavioral-state signal that is coordinated across the dorsal cortex. *Elife* **12**, doi:10.7554/eLife.81826 (2023).

10 Neyhart, E. *et al.* Cortical acetylcholine dynamics are predicted by cholinergic axon activity and behavior state. *Cell Rep* **43**, 114808, doi:10.1016/j.celrep.2024.114808 (2024).

11 Chen, N., Sugihara, H. & Sur, M. An acetylcholine-activated microcircuit drives temporal dynamics of cortical activity. *Nat Neurosci* **18**, 892-902, doi:10.1038/nn.4002 (2015).

12 Chubykin, A. A., Roach, E. B., Bear, M. F. & Shuler, M. G. A cholinergic mechanism for reward timing within primary visual cortex. *Neuron* **77**, 723-735, doi:10.1016/j.neuron.2012.12.039 (2013).

13 Hangya, B., Ranade, S. P., Lorenc, M. & Kepecs, A. Central Cholinergic Neurons Are Rapidly Recruited by Reinforcement Feedback. *Cell* **162**, 1155-1168, doi:10.1016/j.cell.2015.07.057 (2015).

14 Jiang, L. *et al.* Cholinergic Signaling Controls Conditioned Fear Behaviors and Enhances Plasticity of Cortical-Amygdala Circuits. *Neuron* **90**, 1057-1070, doi:10.1016/j.neuron.2016.04.028 (2016).

15 Luchicchi, A., Bloem, B., Viana, J. N., Mansvelder, H. D. & Role, L. W. Illuminating the role of cholinergic signaling in circuits of attention and emotionally salient behaviors. *Front Synaptic Neurosci* **6**, 24, doi:10.3389/fnsyn.2014.00024 (2014).

16 Parikh, V., Kozak, R., Martinez, V. & Sarter, M. Prefrontal acetylcholine release controls cue detection on multiple timescales. *Neuron* **56**, 141-154, doi:10.1016/j.neuron.2007.08.025 (2007).

17 Espinosa, J. S. & Stryker, M. P. Development and plasticity of the primary visual cortex. *Neuron* **75**, 230-249, doi:10.1016/j.neuron.2012.06.009 (2012).

18 Sawtell, N. B. *et al.* NMDA receptor-dependent ocular dominance plasticity in adult visual cortex. *Neuron* **38**, 977-985, doi:Doi 10.1016/S0896-6273(03)00323-4 (2003).

19 Cooke, S. F. & Bear, M. F. Visual Experience Induces Long-Term Potentiation in the Primary Visual Cortex. *Journal of Neuroscience* **30**, 16304-16313, doi:10.1523/Jneurosci.4333-10.2010 (2010).

20 Zhang, L. I., Bao, S. & Merzenich, M. M. Persistent and specific influences of early acoustic environments on primary auditory cortex. *Nat Neurosci* **4**, 1123-1130, doi:10.1038/nn745 (2001).

21 Polley, D. B., Steinberg, E. E. & Merzenich, M. M. Perceptual learning directs auditory cortical map reorganization through top-down influences. *Journal of Neuroscience* **26**, 4970-4982, doi:10.1523/Jneurosci.3771-05.2006 (2006).

22 Gdalyahu, A. *et al.* Associative fear learning enhances sparse network coding in primary sensory cortex. *Neuron* **75**, 121-132, doi:10.1016/j.neuron.2012.04.035 (2012).

23 Shuler, M. G. & Bear, M. F. Reward timing in the primary visual cortex. *Science* **311**, 1606-1609, doi:10.1126/science.1123513 (2006).
24 Faulkner, A. D. *et al.* Context flexibly modulates cue representations in visual cortex. *Nat Commun* **16**, 5516, doi:10.1038/s41467-025-61314-y (2025).
25 Alitto, H. J. & Dan, Y. Cell-type-specific modulation of neocortical activity by basal forebrain input. *Front Syst Neurosci* **6**, 79, doi:10.3389/fnsys.2012.00079 (2012).
26 Gulledge, A. T., Park, S. B., Kawaguchi, Y. & Stuart, G. J. Heterogeneity of phasic cholinergic signaling in neocortical neurons. *J Neurophysiol* **97**, 2215-2229, doi:10.1152/jn.00493.2006 (2007).
27 Kawaguchi, Y. Selective cholinergic modulation of cortical GABAergic cell subtypes. *J Neurophysiol* **78**, 1743-1747, doi:10.1152/jn.1997.78.3.1743 (1997).
28 Bastos, G. *et al.* Top-down input modulates visual context processing through an interneuron-specific circuit. *Cell Reports* **42**, doi:ARTN 113133
10.1016/j.celrep.2023.113133 (2023).
29 Poorthuis, R. B., Enke, L. & Letzkus, J. J. Cholinergic circuit modulation through differential recruitment of neocortical interneuron types during behaviour. *J Physiol-London* **592**, 4155-4164, doi:10.1113/jphysiol.2014.273862 (2014).
30 LeDoux, J. E. Emotion circuits in the brain. *Annu Rev Neurosci* **23**, 155-184, doi:10.1146/annurev.neuro.23.1.155 (2000).
31 Tovote, P., Fadok, J. P. & Lüthi, A. Neuronal circuits for fear and anxiety. *Nature Reviews Neuroscience* **16**, 317-331, doi:10.1038/nrn3945 (2015).
32 Polley, D. B., Heiser, M. A., Blake, D. T., Schreiner, C. E. & Merzenich, M. M. Associative learning shapes the neural code for stimulus magnitude in primary auditory cortex. *Proc Natl Acad Sci U S A* **101**, 16351-16356, doi:10.1073/pnas.0407586101 (2004).
33 Weinberger, N. M. Specific long-term memory traces in primary auditory cortex. *Nat Rev Neurosci* **5**, 279-290, doi:10.1038/nrn1366 (2004).
34 Reed, A. *et al.* Cortical Map Plasticity Improves Learning but Is Not Necessary for Improved Performance. *Neuron* **70**, 121-131, doi:10.1016/j.neuron.2011.02.038 (2011).
35 Metherate, R. & Ashe, J. H. Basal Forebrain Stimulation Modifies Auditory-Cortex Responsiveness by an Action at Muscarinic Receptors. *Brain Res* **559**, 163-167, doi:Doi 10.1016/0006-8993(91)90301-B (1991).
36 Ji, W., Gao, E. & Suga, N. Effects of acetylcholine and atropine on plasticity of central auditory neurons caused by conditioning in bats. *J Neurophysiol* **86**, 211-225, doi:10.1152/jn.2001.86.1.211 (2001).
37 Abs, E. *et al.* Learning-Related Plasticity in Dendrite-Targeting Layer 1 Interneurons. *Neuron* **100**, 684-699 e686, doi:10.1016/j.neuron.2018.09.001 (2018).
38 d'Aquin, S. *et al.* Compartmentalized dendritic plasticity during associative learning. *Science* **376**, eabf7052, doi:10.1126/science.abf7052 (2022).
39 Letzkus, J. J., Wolff, S. B. & Luthi, A. Disinhibition, a Circuit Mechanism for Associative Learning and Memory. *Neuron* **88**, 264-276, doi:10.1016/j.neuron.2015.09.024 (2015).
40 Schroeder, A. *et al.* Inhibitory top-down projections from zona incerta mediate neocortical memory. *Neuron* **111**, 727-738 e728, doi:10.1016/j.neuron.2022.12.010 (2023).
41 Benisty, H. *et al.* Rapid fluctuations in functional connectivity of cortical networks encode spontaneous behavior. *Nature Neuroscience*, doi:10.1038/s41593-023-01498-y (2023).
42 Cardin, J. A., Crair, M. C. & Higley, M. J. Mesoscopic Imaging: Shining a Wide Light on Large-Scale Neural Dynamics. *Neuron* **108**, 33-43, doi:10.1016/j.neuron.2020.09.031 (2020).
43 Barson, D. *et al.* Simultaneous mesoscopic and two-photon imaging of neuronal activity in cortical circuits. *Nat Methods* **17**, 107-113, doi:10.1038/s41592-019-0625-2 (2020).
44 Chen, T. W. *et al.* Ultrasensitive fluorescent proteins for imaging neuronal activity. *Nature* **499**, 295-300, doi:10.1038/nature12354 (2013).
45 Hamodi, A. S., Martinez Sabino, A., Fitzgerald, N. D., Moschou, D. & Crair, M. C. Transverse sinus injections drive robust whole-brain expression of transgenes. *Elife* **9**, doi:10.7554/eLife.53639 (2020).
46 Wekselblatt, J. B., Flister, E. D., Piscopo, D. M. & Niell, C. M. Large-scale imaging of cortical dynamics during sensory perception and behavior. *J Neurophysiol* **115**, 2852-2866, doi:10.1152/jn.01056.2015 (2016).

47 Harris, K. D., Quiroga, R. Q., Freeman, J. & Smith, S. L. Improving data quality in neuronal population recordings. *Nat Neurosci* **19**, 1165-1174, doi:10.1038/nn.4365 (2016).
48 Ma, Y. *et al.* Wide-field optical mapping of neural activity and brain haemodynamics: considerations and novel approaches. *Philos Trans R Soc Lond B Biol Sci* **371**, doi:10.1098/rstb.2015.0360 (2016).
49 Peron, S., Chen, T. W. & Svoboda, K. Comprehensive imaging of cortical networks. *Curr Opin Neurobiol* **32**, 115-123, doi:10.1016/j.conb.2015.03.016 (2015).
50 Waters, J. Sources of widefield fluorescence from the brain. *Elife* **9**, doi:10.7554/eLife.59841 (2020).
51 Harris, J. A. *et al.* Anatomical characterization of Cre driver mice for neural circuit mapping and manipulation. *Front Neural Circuits* **8**, 76, doi:10.3389/fncir.2014.00076 (2014).
52 Pfeffer, C. K., Xue, M. S., He, M., Huang, Z. J. & Scanziani, M. Inhibition of inhibition in visual cortex: the logic of connections between molecularly distinct interneurons. *Nature Neuroscience* **16**, 1068-U1130, doi:10.1038/nn.3446 (2013).
53 Atallah, B. V., Bruns, W., Carandini, M. & Scanziani, M. Parvalbumin-expressing interneurons linearly transform cortical responses to visual stimuli. *Neuron* **73**, 159-170, doi:10.1016/j.neuron.2011.12.013 (2012).
54 Hofer, S. B. *et al.* Differential connectivity and response dynamics of excitatory and inhibitory neurons in visual cortex. *Nat Neurosci* **14**, 1045-1052, doi:10.1038/nn.2876 (2011).
55 Runyan, C. A. *et al.* Response features of parvalbumin-expressing interneurons suggest precise roles for subtypes of inhibition in visual cortex. *Neuron* **67**, 847-857, doi:10.1016/j.neuron.2010.08.006 (2010).
56 Lee, S. H. *et al.* Activation of specific interneurons improves V1 feature selectivity and visual perception. *Nature* **488**, 379-383, doi:10.1038/nature11312 (2012).
57 Ferguson, K. A. *et al.* VIP interneurons regulate cortical size tuning and visual perception. *Cell Rep* **42**, 113088, doi:10.1016/j.celrep.2023.113088 (2023).
58 Keller, A. J. *et al.* A Disinhibitory Circuit for Contextual Modulation in Primary Visual Cortex. *Neuron* **108**, 1181-1193 e1188, doi:10.1016/j.neuron.2020.11.013 (2020).
59 Millman, D. J. *et al.* VIP interneurons in mouse primary visual cortex selectively enhance responses to weak but specific stimuli. *Elife* **9**, doi:10.7554/eLife.55130 (2020).
60 Piet, A. *et al.* Behavioral strategy shapes activation of the Vip-Sst disinhibitory circuit in visual cortex. *Neuron* **112**, 1876-1890 e1874, doi:10.1016/j.neuron.2024.02.008 (2024).
61 Fu, Y. *et al.* A cortical circuit for gain control by behavioral state. *Cell* **156**, 1139-1152, doi:10.1016/j.cell.2014.01.050 (2014).
62 Hartung, J., Schroeder, A., Perez Vazquez, R. A., Poorthuis, R. B. & Letzkus, J. J. Layer 1 NDNF interneurons are specialized top-down master regulators of cortical circuits. *Cell Rep* **43**, 114212, doi:10.1016/j.celrep.2024.114212 (2024).
63 Malina, K. C. K. *et al.* NDNF interneurons in layer 1 gain-modulate whole cortical columns according to an animal's behavioral state. *Neuron* **109**, 2150-+, doi:10.1016/j.neuron.2021.05.001 (2021).
64 Naumann, L. B., Hertag, L., Muller, J., Letzkus, J. J. & Sprekeler, H. Layer-specific control of inhibition by NDNF interneurons. *Proc Natl Acad Sci U S A* **122**, e2408966122, doi:10.1073/pnas.2408966122 (2025).
65 Schuman, B., Dellal, S., Pronneke, A., Machold, R. & Rudy, B. Neocortical Layer 1: An Elegant Solution to Top-Down and Bottom-Up Integration. *Annu Rev Neurosci* **44**, 221-252, doi:10.1146/annurev-neuro-100520-012117 (2021).
66 Schuman, B. *et al.* Four Unique Interneuron Populations Reside in Neocortical Layer 1. *J Neurosci* **39**, 125-139, doi:10.1523/JNEUROSCI.1613-18.2018 (2019).
67 Dimidschstein, J. *et al.* A viral strategy for targeting and manipulating interneurons across vertebrate species. *Nat Neurosci* **19**, 1743-1749, doi:10.1038/nn.4430 (2016).
68 Herrero, J. L. *et al.* Acetylcholine contributes through muscarinic receptors to attentional modulation in V1. *Nature* **454**, 1110-1114, doi:10.1038/nature07141 (2008).
69 James, N. M., Gritton, H. J., Kopell, N., Sen, K. & Han, X. Muscarinic receptors regulate auditory and prefrontal cortical communication during auditory processing. *Neuropharmacology* **144**, 155-171, doi:10.1016/j.neuropharm.2018.10.027 (2019).
70 Kang, J. I. & Vaucher, E. Cholinergic Pairing with Visual Activation Results in Long-Term Enhancement of Visual Evoked Potentials. *Plos One* **4**, doi:ARTN e5995

10.1371/journal.pone.0005995 (2009).

71 Kilgard, M. P. & Merzenich, M. M. Cortical map reorganization enabled by nucleus basalis activity. *Science* **279**, 1714-1718, doi:10.1126/science.279.5357.1714 (1998).

72 Zelikowsky, M. *et al*. Cholinergic Blockade Frees Fear Extinction from Its Contextual Dependency. *Biol Psychiat* **73**, 345-352, doi:10.1016/j.biopsych.2012.08.006 (2013).

73 Jing, M. *et al*. An optimized acetylcholine sensor for monitoring in vivo cholinergic activity. *Nat Methods* **17**, 1139-1146, doi:10.1038/s41592-020-0953-2 (2020).

74 Disney, A. A. & Higley, M. J. Diverse Spatiotemporal Scales of Cholinergic Signaling in the Neocortex. *J Neurosci* **40**, 720-725, doi:10.1523/JNEUROSCI.1306-19.2019 (2020).

75 Sarter, M. & Lustig, C. Cholinergic double duty: cue detection and attentional control. *Curr Opin Psychol* **29**, 102-107, doi:10.1016/j.copsyc.2018.12.026 (2019).

76 Reimer, J. *et al*. Pupil fluctuations track rapid changes in adrenergic and cholinergic activity in cortex. *Nat Commun* **7**, 13289, doi:10.1038/ncomms13289 (2016).

77 Zou, J. *et al*. Goal-directed motor actions drive acetylcholine dynamics in sensory cortex. *Elife*, doi:https://doi.org/10.7554/eLife.96931.1 (2024).

78 Hegedus, P. *et al*. Parvalbumin-expressing basal forebrain neurons mediate learning from negative experience. *Nat Commun* **15**, 4768, doi:10.1038/s41467-024-48755-7 (2024).

79 Robert, B. *et al*. A functional topography within the cholinergic basal forebrain for encoding sensory cues and behavioral reinforcement outcomes. *Elife* **10**, doi:ARTN e69514

10.7554/eLife.69514

10.7554/eLife.69514.sa0

10.7554/eLife.69514.sa1

10.7554/eLife.69514.sa2 (2021).

80 Acquas, E., Wilson, C. & Fibiger, H. C. Conditioned and unconditioned stimuli increase frontal cortical and hippocampal acetylcholine release: effects of novelty, habituation, and fear. *J Neurosci* **16**, 3089-3096, doi:10.1523/JNEUROSCI.16-09-03089.1996 (1996).

81 Howe, W. M. *et al*. Acetylcholine Release in Prefrontal Cortex Promotes Gamma Oscillations and Theta-Gamma Coupling during Cue Detection. *J Neurosci* **37**, 3215-3230, doi:10.1523/JNEUROSCI.2737-16.2017 (2017).

82 Gritton, H. J. *et al*. Cortical cholinergic signaling controls the detection of cues. *Proc Natl Acad Sci U S A* **113**, E1089-1097, doi:10.1073/pnas.1516134113 (2016).

83 Meir, I., Katz, Y. & Lampl, I. Membrane Potential Correlates of Network Decorrelation and Improved SNR by Cholinergic Activation in the Somatosensory Cortex. *J Neurosci* **38**, 10692-10708, doi:10.1523/JNEUROSCI.1159-18.2018 (2018).

84 Pinto, L. *et al*. Fast modulation of visual perception by basal forebrain cholinergic neurons. *Nat Neurosci* **16**, 1857-1863, doi:10.1038/nn.3552 (2013).

85 Chaves-Coira, I., Barros-Zulaica, N., Rodrigo-Angulo, M. & Nunez, A. Modulation of Specific Sensory Cortical Areas by Segregated Basal Forebrain Cholinergic Neurons Demonstrated by Neuronal Tracing and Optogenetic Stimulation in Mice. *Front Neural Circuits* **10**, 28, doi:10.3389/fncir.2016.00028 (2016).

86 Kim, J. H. *et al*. Selectivity of Neuromodulatory Projections from the Basal Forebrain and Locus Ceruleus to Primary Sensory Cortices. *J Neurosci* **36**, 5314-5327, doi:10.1523/JNEUROSCI.4333-15.2016 (2016).

87 Li, X. *et al*. Generation of a whole-brain atlas for the cholinergic system and mesoscopic projectome analysis of basal forebrain cholinergic neurons. *Proc Natl Acad Sci U S A* **115**, 415-420, doi:10.1073/pnas.1703601115 (2018).

88 Zaborszky, L. *et al*. Neurons in the Basal Forebrain Project to the Cortex in a Complex Topographic Organization that Reflects Corticocortical Connectivity Patterns: An Experimental Study Based on Retrograde Tracing and 3D Reconstruction. *Cereb Cortex* **25**, 118-137, doi:10.1093/cercor/bht210 (2015).

89 Knudstrup, S. G. *et al*. Visual stimulation drives retinotopic acetylcholine release in the mouse visual cortex. *bioRxiv*, doi:https://doi.org/10.1101/2024.02.04.578821 (2024).

90 Kuhlman, S. J. *et al*. A disinhibitory microcircuit initiates critical-period plasticity in the visual cortex. *Nature* **501**, 543-546, doi:10.1038/nature12485 (2013).

91 Makino, H. & Komiyama, T. Learning enhances the relative impact of top-down processing in the visual cortex. *Nat Neurosci* **18**, 1116-1122, doi:10.1038/nn.4061 (2015).

92 Poort, J. *et al*. Learning Enhances Sensory and Multiple Non-sensory Representations in Primary Visual Cortex. *Neuron* **86**, 1478-1490, doi:10.1016/j.neuron.2015.05.037 (2015).

93 Brombas, A., Fletcher, L. N. & Williams, S. R. Activity-Dependent Modulation of Layer 1 Inhibitory Neocortical Circuits by Acetylcholine. *Journal of Neuroscience* **34**, 1932-1941, doi:10.1523/Jneurosci.4470-13.2014 (2014).

94 Sweeney, C. G. *et al*. Reliable sensory processing of superficial cortical interneurons is modulated by behavioral state. *Cell Reports* **44**, doi:ARTN 115678
10.1016/j.celrep.2025.115678 (2025).

Figure Legends

Figure 1: **Visually-cued lick suppression is rapidly induced and dependent on visual cortex activity**. (**a**) Schematic of the behavioral setup. During conditioning, a 5-second filtered noise stimulus is followed by a 1-second trace and a 0.5-second foot-shock. Below are example traces of the visual stimulus presentation, foot-shock, and lick-rate from a portion of a post-conditioning session. (**b**) Normalized lick indices per day, with day 0 as the first session where the conditioned stimulus was paired with foot-shock (n=17 mice). (**c**) Average pre- and post-conditioning lick indices (n=17 mice, session averages from each mouse are shown in gray) * indicates $p<0.05$, paired t-test. (**d**) Example lick raster aligned to visual stimulus onset (gray bar) across pre- and post-conditioning, muscimol session (musc), and post-muscimol session. (**e**) Average pre, post conditioning, muscimol session, and post muscimol session conditioning lick indices (n=7 mice) * indicates $p<0.05$ for pairwise post-hoc comparisons (Tukey-Kramer corrected) against pre-conditioning session following a significant ($p<0.05$) main effect of session in repeated measures ANOVA. For panels **b**,**c**, & **e**, data are represented as mean ± SEM.

Figure 2: Visual fear-conditioning enhances visually-evoked activity. (**a**) Schematic of the widefield imaging setup. (**b**) Top: example transcranial imaging field of view showing GCaMP6 expression. Scale bar: 1mm. Bottom: averaged retinotopic field sign maps with Allen CCFv3 parcels overlaid in white. (**c**) Example time series from a portion of a post-conditioning session showing onsets of visual stimuli, lick-rate, and traces corresponding to calcium activity in Allen parcels (VisP; primary visual cortex, RSC; retrosplenial cortex, SS_{bfd}; somatosensory cortex barrel field, M1; primary motor cortex). (**d**) Example image frames showing the visual stimulus response post-conditioning from the gray segment in (**c**). Times in seconds are relative to visual stimulus onset at t=0s (indicated in (**c**) by the red arrowhead). White lines indicate Allen CCFv3-derived parcellation. (**e**) Traces show visual stimulus-averaged activity pre- and post-conditioning from the Allen parcels in (**c**) (n=7 mice). (**f**) Average spatial map of the difference (post minus pre-conditioning) in the visual response amplitude for each Allen parcel (n=7 mice). (**g**) Average response in VisP parcel pre- and post-conditioning (n=7 mice) * indicates $p<0.05$, paired t-test. (**h**) Schematic of the 2-photon imaging setup. (**i**) Top: example 2-photon imaging field of view. Scale bar, 100 μm. Bottom: averaged retinotopic field sign maps with Allen CCFv3 parcels overlaid in white. (**j**) Example time series from one animal from a portion of a post-conditioning session showing onsets of visual stimuli, lick-rate, and traces corresponding to selected cell regions of interest. (**k**) Left: Averaged stimulus-aligned visual response pre- and post-conditioning in excitatory cells. Right: Average response amplitude pre- and post-conditioning (n=4 mice). * indicates $p<0.05$, paired t-test. For panels **e**,**g**, & **k**, data are represented as mean ± SEM.

Figure 3: GABAergic plasticity following visual fear conditioning. (**a**) Schematic of local cortical circuitry. (**b**) Left: averaged retinotopic field sign map in GCaMP6s expressing PV-Cre mice (n=5 mice). Right: confocal image of GCaMP6s-expressing PV-INs in layer 2/3 in an example PV-Cre mouse. Scale bar, 70 μm. Below is

an example 2-photon field of view. Scale bar, 50 μm. (**c**) Example time series from one animal from a segment of a post-conditioning session showing onsets of visual stimuli, lick-rate, and traces corresponding to selected cell regions of interest. (**d**) Left: Averaged stimulus-aligned visual response pre- and post-conditioning in PV-INs. Gray box indicates the time of the visual stimulus. Right: Average response amplitude during the visual response (n=5 mice). (**e-g**) Same as in (**d**) for SST-INs, VIP-INs and L1-INs (n=6 SST-Cre mice; n=4 VIP-Cre mice; n=3 mDLX-GCaMP6f L1 mice). * indicates p<0.05, paired t-test. For panels **d**,**e**,**f**,**g**, data are represented as mean ± SEM.

Figure 4: Cholinergic plasticity following visual fear conditioning. (**a**) Schematic of the widefield imaging setup. (**b**) Top: Example transcranial imaging field of view showing $GRABS_{ACh}$ expression. Scale bar: 1mm. Bottom: Averaged, intrinsic-imaging derived, retinotopic field sign maps with Allen CCFv3 parcels overlaid in white. (**c**) Example time series from one animal from a segment of a post-conditioning session showing onsets of visual stimuli, lick-rate, and traces corresponding to $GRABS_{ACh}$ activity in Allen parcels (VisP; primary visual cortex, RSC; retrosplenial cortex, SS_{bfd}; somatosensory cortex barrel field, M1; primary motor cortex). (**d**) Example image frames showing the visual stimulus response post-conditioning from the gray segment in (**c**). Times in seconds are relative to visual stimulus onset at t=0s (indicated in (**c**) by the red arrowhead). White lines indicate Allen CCFv3-derived parcellation. (**e**) Traces show visual stimulus-averaged activity pre- and post-conditioning (n=7 mice) from the Allen parcels in (**c**). (**f**) Average spatial map of the difference (post-preconditioning) in the visual response for each Allen parcel (n=7 mice). (**g**) Average $GRABS_{Ach}$ response in VisP parcel pre- and post-conditioning (n=7 mice). * indicates p<0.05, paired t-test. (**h**) Top: example transcranial imaging field of view showing GCaMP8 expression three weeks after AAV injection. Red arrowheads indicate locations of craniotomies for local pharmacology experiments. Scale bar: 1mm. Bottom: averaged retinotopic field sign maps with Allen CCFv3 parcels overlaid in white. (**i**) Example lick raster aligned to visual stimulus onset (gray bar) across pre- and post-conditioning, a scopolamine session (scop), and a post-scopolamine, vehicle session. (**j**) Average pre-, post-conditioning, scopolamine session, and vehicle session conditioning lick indices (n=4 mice). * indicates p<0.05 for pairwise post-hoc comparisons (Tukey-Kramer corrected) against pre-conditioning session following a significant (p<0.05) main effect of session in repeated measures ANOVA. (**k**) Traces show visual stimulus-averaged activity post-conditioning from visual cortex after local injection of either scopolamine or vehicle (n=4 mice). (**l**) Magnitude of visual response (Scopolamine/vehicle) pre- and post-conditioning. * indicates p<0.05 for one-sample t-test comparing population response to hypothesized mean of 1. For **e**,**g**,**j**,**k**, & **l** data are represented as mean ± SEM.

Methods

Animals

Male and female mice (C57BL/6J, Slc17a7-Cre; Jax stock no. 037512 crossed to Ai148; Jax stock no 030238, VIP-IRES-Cre$^{+/0}$; Jax stock no. 031628, SST-IRES-Cre$^{+/0}$; Jax stock no. 018973, PV-IRES-Cre$^{+/0}$; Jax stock no. 008069) were kept on a 12h light/dark cycle and provided with ad libitum food and water prior to surgery and/or conditioning experiments. Animals were individually housed following head-post implants. All behavioral and imaging experiments were performed during the light phase of the cycle. All animal handling and experiments were performed according to the ethical guidelines of the Institutional Animal Care and Use Committee of the Yale University School of Medicine.

Neonatal sinus injections

In a subset of experimental animals, brain-wide expression of the GRABS$_{ACh}$ Sensor and/or calcium indicators (jGCaMP6s) was achieved via postanal sinus injections as previously described [1,2]. Neonatal pups (postnatal day 0-1) were injected with 8µl (4 µl per hemisphere) with AAV9-Syn-GRABS$_{ACh}$ and/or AAV9-Syn-GCaMP6s-WPRE-SV40 (Addgene no. 100843).

Surgical procedures

All other surgical procedures were performed on adult mice (between P50 and P180). Mice were anesthetized using 1-2% isoflurane and maintained at 37°C for the duration of the surgery. For widefield imaging implants, the skin and fascia over the skull were removed from the nasal bone to the posterior of the intraparietal bone and laterally between the temporal muscles. The surface of the skull was cleaned with saline and gently polished with wool buffing pads. The edges of the incision were secured to the skull with tissue glue (Vetbond, 3M). A custom titanium headpost was secured to the posterior of the nasal bone with transparent dental cement (C&B Metabond, Butler Schein). A thin layer of cyanoacrylate (Maxi-Cure, Bob Smith Industries) was used to cover the skull and left to cure for at least 30 minutes at room temperature to provide a smooth surface for transcranial imaging.

In IRES-Cre mice, injections of AAV9-Syn-FLEX-GCaMP6s-WPRE-SV40 (Addgene no. 100845, diluted to a titer of 2.5x10^12 vg/mL) were targeted to V1. For layer 1 imaging experiments, 500 nL of AAV9-mDlx-GCaMP6f-Fishell-2 (Addgene no. 83899, diluted to a titer of 2.2x10^12 vg/mL) were targeted to V1. A subset of mice was locally injected with AAV9-CamKIIa-jGCaMP8m-WPRE (Addgene no. 176751, diluted to a titer of 2x10^12 vg/mL). All viral injections (600-800 nL) were made via a beveled glass micropipette at a rate of 1-2 nL/second into V1 layer 2/3 (between 150-300 µm in depth) using a Nanoject III (Drummond). After injections, pipettes were left in the brain for more than 10 minutes to prevent backflow.

For two-photon calcium imaging implants, mice were anesthetized, and the scalp was cleaned with Betadine and 70% ethanol. The scalp was removed, and the fascia over the skull was cleaned with saline. A custom titanium headpost was secured to the skill with opaque dental cement (C&B Metabond, Butler Schein). A 3 mm^2 craniotomy was made over V1, and a glass window, consisting of a 3 mm^2 inner coverslip adhered with ultraviolet-curing adhesive (Norland Optical Adhesives #81) to a 5 mm^2 outer coverslip (both #1 Warner Instruments), was inserted into the craniotomy and secured with cyanoacrylate glue (Loctite). Metabond was applied to cover any remaining exposed skull. Analgesics were given immediately after surgery (5 mg/kg Carprofen) and on the following two days to aid recovery. Mice were maintained on an antibiotic diet (Sulfatrim, Butler Schein) to prevent infection and allowed to recover for at least 5 days before subsequent handling and behavioral experiments.

Histology

Histology was performed on a subset of animals at the conclusion of imaging and behavioral experiments to confirm indicator expression. Mice were deeply anesthetized with isoflurane and perfused intracardially with phosphate-buffered saline (PBS) followed by 4% paraformaldehyde in PBS. Brains were postfixed overnight at 4°C and subsequently stored in PBS. Tissue was sectioned at 50 µm using a vibrating blade vibratome (Leica VT 1000 S), mounted onto slides, and visualized via light microscopy. Widefield epifluorescence images and confocal images were taken with a Zeiss LSM 900.

Widefield imaging

Imaging was performed using a Zeiss Axio Zoom microscope with a 1x, 0.25 numerical aperture objective. Widefield excitation light was from an LED bank (Spectra X Light Engine, Lumencor). Emitted light passed through an image splitter (TwinCam, Cairn Research), then through a 525/50nm ($GRABS_{Ach}$ or GCaMP6s) filter (Chroma) before it reached a sCMOS camera (Orca-Flash V3, Hamamatsu). Images were acquired with an 18-20x digital zoom at 512x512 resolution after 4x pixel binning. Each channel was acquired at 10 Hz with a 35-ms exposure using HCImage software (Hamamatsu).

Retinotopic mapping and visual stimulation

Before the start of behavioral experiments, cortical visual areas were mapped using a filtered noise stimulus that drifted across the visual field of head-fixed animals [3]. All visual stimuli were generated using Psychtoolbox-3 in MATLAB and presented on a gamma-calibrated LCD monitor (Acer V206HQL, 17 inches, spatial resolution of 1600x900, frame refresh rate of 60 Hz, mean luminance of 20 cd/m^2) positioned 20 cm away from and parallel to the left eye. Filtered noise had a temporal frequency of 2 Hz and a spatial frequency of 0.04 cycles per degree and drifted 20 times along each cardinal axis at rates of 0.086 Hz (altitude) and 0.063 Hz (azimuth). Corrective distortion was applied to the drifting stimuli to alleviate the distortion caused by using a flat monitor to cover a large visual angle. To ensure that stimulus-evoked activity had subsided between sweeps, a gap of 2 seconds was inserted between stimuli. To generate visual field sign maps, we created stimulus-triggered mean $\Delta F/F_0$

movies using the 2-second intersweep interval as the F_0. A fast Fourier transform (FFT) was used to generate altitude and azimuth phase maps. Then the visual field sign at each pixel was calculated as the sine of the angle between local gradients derived from the phase maps. In conditioning experiments, we presented 5-second, full-screen noise stimuli with the same parameters described above on the same LCD monitor. In a subset of post-conditioning experiments, the contrast of the noise stimulus was randomly varied between one, two, five, ten, and one hundred percent contrast. In discriminative conditioning experiments, the conditioned stimuli were 80-degree drifting gratings (2 Hz, 0.04 cycles per degree) with the CS-plus oriented vertically and the CS-minus oriented horizontally.

Two-photon imaging

Two-photon imaging was performed using a MOM microscope (Sutter Instruments) coupled to a 16x, 0.8 numerical aperture objective (Nikon). Excitation light was delivered by a titanium-sapphire laser (Mai Tai eHP DeepSee, Spectra-Physics) tuned to 920 nm. Emitted light was collected through a 525/50 nm filter, then a gallium arsenide phosphide photomultiplier tube (Hamamatsu). Images were acquired at 512x512 resolution (with 2x digital zoom) at 30 Hz using a galvo-resonant scan system controlled by ScanImage software (Vidrio). Imaging was performed at a depth of 120-250 μm for layer 2/3 neurons or 20-100 μm for layer 1 neurons. For each animal, only one field of view (FOV) was imaged, chosen to include V1 based on widefield area border maps and blood vessel markers that were observed and registered between functional maps and 2-photon fields of view. Imaging FOVs were matched across days using the template image and z-coordinates from the initial imaging session.

Behavioral monitoring

All experiments were performed in awake, behaving mice that were head-fixed. During widefield and two-photon imaging experiments, the animal's face was illuminated with an infrared LED bank and imaged with a miniature CMOS camera (Blackfly S USB3, FLIR) with a frame rate of 10 Hz. Video was acquired with SpinView software (FLIR).

Behavioral conditioning

For all experiments, animals were habituated to being head-fixed for at least 5 days prior to the start of conditioning. During this period, mice were water-restricted to no less than 85% of their initial body weight and trained to lick for rewards (a 1% sucrose solution) at a waterspout coupled to a fiber-optic sensor that detected beam breaks (OPTEX NF-DT05). Licks events were monitored by custom MATLAB software. Detected licks triggered a solenoid valve to deliver a 2μl reward and start a subsequent random time interval (1 to 3 seconds) in which no further reward could be delivered. After mice demonstrated consistent licking throughout head-fixation sessions, we began pre-conditioning sessions in which 10-20 visual stimuli (5-second filtered noise, see visual stimulation section for details) were delivered with an inter-stimulus interval drawn from an exponential distribution (ranging from 50 to 150 seconds, such that mice could not predict the timing of the subsequent trials).

After three pre-conditioning sessions, visual stimuli were paired with a 0.5-second, 0.2-0.4 mA foot-shock passed between two grounding braids (Molex) under the animal via a precision-regulated shocker (H13015, Coulbourn Instruments) in two-pole (bipolar) current reversal square wave output mode. The offset of the visual stimulus was followed by a 1-second trace before the onset of the foot-shock. The timing of the shock and visual stimulus was coordinated with custom MATLAB codes through a NI-DAQmx board (PCIe-6315, National Instruments), and all output timing signals were acquired with a Power 1401 digitizer (Cambridge Electronic Design) and sampled at 5 kHz. During conditioning, animals were constantly monitored, and sessions were terminated if signs of stress were observed (e.g., vocalizations, excessive struggling). Mice were trained daily, with sessions lasting approximately 20 minutes.

Pharmacology

Animals were injected with either sterile saline or scopolamine hydrobromide (1 mg/kg, i.p., Tocris Bioscience; CAS no. 114-49-8) 15 minutes before behavioral sessions. For acute, local injections of muscimol (1 µg/µL, Tocris Bioscience; CAS no. 2763-96-4, dissolved in ACSF), craniotomies were made bilaterally over V1 and covered with silicone sealant (Kwik-cast, WPI) at least one day prior to behavioral sessions. 15 min prior to behavior sessions, mice were head-fixed and injected locally. For acute local scopolamine experiments, craniotomies were targeted to V1 after functional area mapping but prior to behavioral training. During acute injection sessions, 500-600 uL of scopolamine (0.2 mM) was injected into visual cortex at a rate of 1-2 nL/second in awake, head fixed animals, free to run on a wheel under a stereotaxic arm. Animals were left to recover for 15 min in their home cage before head fixation in the behavioral/imaging apparatus.

Data analysis

All analyses were conducted using custom-written scripts in MATLAB (Mathworks) with motion correction performed using the NoRMCorre software package [4]. No statistical methods were used to predetermine sample sizes. All animals were randomly selected from our colony for inclusion in the study.

Preprocessing of behavior data:

Pupil area and facial movements (dominated mainly by lick-related activity) were extracted from face videos using FaceMap [5].

Preprocessing of licking behavior:

To measure lick suppression, we used a normalized lick index [6,7] comparing the number of licks during the 5-second baseline period preceding the 5-second visual stimulus and the number of licks during the visual stimulus ($licks_{vis}$-$licks_{baseline}$/$licks_{vis}$+$licks_{baseline}$). To estimate lick rates, lick times were convolved with a Gaussian filter (with a 1-second smoothing window), and the lick density was interpolated to match the sampling rate of other simultaneously acquired timing signals (5 kHz).

Preprocessing of widefield imaging data:

Widefield images were processed as previously described [1,2]. Briefly, detrending was applied using a low-pass filter ($N = 100$, $fcutoff = 0.001$ Hz). Time traces were obtained using $(\Delta F/F)_i = (F_i - F_{i,0})/F_{i,0}$, where F_i is the fluorescence of pixel i and $F_{i,0}$ is the corresponding low-pass-filtered signal. To register widefield movies to the Allen Common Coordinate Framework (CCFv3) [8], we used field sign maps from visual area mapping sessions to ensure that V1 was well circumscribed by the 'VisP' Allen parcel. Subsequent imaging sessions were aligned to the retinotopic mapping session using a rigid, intensity-based registration (imregtform in MATLAB), which utilized raw images from both the retinotopic mapping session and the behavioral imaging sessions. Hemodynamic correction was applied as described in Lohani, Moberly et al. (2022) using the approximate isosbestic excitation of GCaMP6s or $GRABS_{ACh}$ to estimate activity-independent fluctuations in fluorescence. Final activity traces were obtained by z-scoring the corrected ΔF/F signals per pixel.

Quantification of two-photon signals:

Analysis of 2-photon imaging data was performed using custom routines in MATLAB. Motion artifacts were corrected using NoRMCorre, and regions of interest (ROIs) were selected as previously described [9]. All pixels in each ROI were averaged as a measure of fluorescence, and the neuropil signal was subtracted. Visually evoked ΔF/F was calculated as $(F-F_0)/F_0$, where F_0 was the mean fluorescence in the 3 seconds preceding visual stimulation. Evoked response amplitudes were quantified as the mean over the first second of the visual stimulus.

Data availability

The full datasets generated and analyzed in this study are available from the corresponding authors on request due to the large volume of data.

Code availability

Code used in analysis is available at GitHub: https://github.com/cardin-higley-lab

Methods references

1 Benisty, H. *et al*. Rapid fluctuations in functional connectivity of cortical networks encode spontaneous behavior. *Nature Neuroscience*, doi:10.1038/s41593-023-01498-y (2023).

2 Lohani, S. *et al*. Spatiotemporally heterogeneous coordination of cholinergic and neocortical activity. *Nat Neurosci* **25**, 1706-1713, doi:10.1038/s41593-022-01202-6 (2022).

3 Zhuang, J. *et al*. An extended retinotopic map of mouse cortex. *Elife* **6**, doi:10.7554/eLife.18372 (2017).

4 Pnevmatikakis, E. A. & Giovannucci, A. NoRMCorre: An online algorithm for piecewise rigid motion correction of calcium imaging data. *J Neurosci Methods* **291**, 83-94, doi:10.1016/j.jneumeth.2017.07.031 (2017).

5 Syeda, A. *et al*. Facemap: a framework for modeling neural activity based on orofacial tracking. *Nat Neurosci* **27**, 187-195, doi:10.1038/s41593-023-01490-6 (2024).

6 Ahmed, M. S. *et al*. Hippocampal Network Reorganization Underlies the Formation of a Temporal Association Memory. *Neuron* **107**, 283-291 e286, doi:10.1016/j.neuron.2020.04.013 (2020).

7 Yu, K., Garcia da Silva, P., Albeanu, D. F. & Li, B. Central Amygdala Somatostatin Neurons Gate Passive and Active Defensive Behaviors. *J Neurosci* **36**, 6488-6496, doi:10.1523/JNEUROSCI.4419-15.2016 (2016).

8 Wang, Q. *et al*. The Allen Mouse Brain Common Coordinate Framework: A 3D Reference Atlas. *Cell* **181**, 936-953 e920, doi:10.1016/j.cell.2020.04.007 (2020).

9 Chen, T. W. *et al*. Ultrasensitive fluorescent proteins for imaging neuronal activity. *Nature* **499**, 295-300, doi:10.1038/nature12354 (2013).

Acknowledgements

The authors thank all members of the Higley and Cardin laboratories for input throughout all stages of this study. We thank Rima Pant and Estela Murillo for generating adeno-associated virus (AAV) vectors. This work was supported by funding from the NIH (R01EY022951 to J.A.C., R01EY035127 to J.A.C., R01MH113852 to J.A.C. and M.J.H., R01MH099045, R21MH121841, and DP1EY033975 to M.J.H., F32EY031133, and K99EY035344 to A.H.M.

Author contributions

A.H.M, J.A.C., and M.J.H. conceptualized and designed the study. A.H.M. collected and analyzed the data. A.H.M, J.A.C., and M.J.H. wrote the manuscript.

Competing interests declaration

The authors declare no competing interests.

Corresponding author

Correspondence to Jessica A. Cardin or Michael J. Higley

Extended data

Extended Data Figure 1: **Baseline arousal metrics and behavior summary**. (**a**) Histogram of interstimulus intervals across pre- and post-conditioning sessions. Dashed line indicates population mean (55 seconds). (**b**) Average visual-stimulus aligned lick rate from post-conditioning sessions showing timescale of licking recovery after shock (n=17 mice). (**c**) Baseline lick rates (average from the 5-second period before visual stimulus onset) in pre-and post-conditioning sessions (n=17 mice). (**d**) Baseline lick rates during pre-conditioning and muscimol treatment sessions (n=7 mice). (**e**) example pupil images (averaged across the 5-second baseline period) from a pre (top) and post (bottom) conditioning session. (**f**) Pupil area from the baseline period in pre- and post-conditioning sessions (n=15 mice). (**g**) Evoked Z-scored pupil area (normalized to the 5-second baseline period) pre and post conditioning (n=13 mice). (**h**) Evoked pupil response (during the 5-second visual stimulus) pre- and post-conditioning (n=13 mice). * indicates $p<0.05$, paired t-test. (**i**) Normalized lick index as a function of stimulus contrast (n=3 mice). * indicates $p<0.05$, main effect of contrast in repeated measures ANOVA. (**j-k**) Normalized lick indices pre- and post-conditioning for mice used in 1-photon (**j**) and 2-photon (**k**) imaging experiments. * indicates $p<0.05$, paired t-test. For panels **b**,**c**,**d**,**f**,**g**,**h**,**l**,**j**, & **k** data are represented as mean ± SEM.

Extended Data Figure 2: Stimulus-specific plasticity in visual responses (**a**) Difference (post minus pre-conditioning) in the visual response amplitude for all Allen parcels. (**b**) Top: averaged traces aligned to spontaneous lick offsets in imaging sessions during lick-training showing response in visual (VisP) and motor (M1 and M2) Allen parcels. Below: average image frames from the times indicated by the red arrowheads (n=7 mice). (**c**) Schematic for differentially-cued fear conditioning experiments. (**d**) Top: example lick raster aligned to visual stimulus onset (gray bar) from a post-conditioning session. Below shows the trials split into either CS-minus (middle) or CS-Plus (bottom) trials. (**e**) Normalized lick indices per day, with day 0 as the first session where the CS-Plus was paired with footshock (n=9 mice). (**f**) Preference index (CS^{+}-CS^{-} / CS^{+}+CS^{-}) for visual response in VisP Allen parcel pre- and post-conditioning. * indicates $p<0.05$, paired t-test. For panels **a**,**b**,**e**, & **f**, data are represented as mean ± SEM.

Extended Data Figure 3: GABAergic imaging summary. (**a**) Histograms of average visually-evoked cell responses from layer 2/3 PNs (700 cells, 4 mice), PV (100 cells, 5 mice), SST (43 cells, 6 mice), VIP (120 cells, 4 mice), and L1-IN (92 cells, 3 mice). (**b**) Left: averaged retinotopic field sign map in GCaMP6s expressing SST-INs (n=6). Middle: an example 2-photon field of view. Scale bar, 50 μm. Right: confocal image of GCaMP6s-expressing cells in layer 2/3 in an example SST-Cre mouse. Scale bar, 70 μm. (**c**) Example time series from one animal from a segment of a post-conditioning session showing onsets of visual stimuli, lick-rate, and traces corresponding to selected cell regions of interest. (**d-e**) Same as b-c for VIP-INs. (**f-g**) Same as **b-c** for L1-INs. Layer 1 is indicated by dashed lines.

Extended Data Figure 4: **Impact of cholinergic blockers on behavior and baseline activity** (**a**) Difference (post minus pre-conditioning) in the visual response amplitude for all Allen parcels. (**b**) Average visual response pre vs post for motor (M1 and M2) and VisP parcels. * indicates $p<0.05$, paired t-test. (**c**) Averaged traces aligned to spontaneous lick offsets in imaging sessions preceding conditioning showing $GRAB_{ACh}$ response in visual (VisP) and motor (M1 and M2) Allen parcels. Below shows averaged image frame from the time indicated by the red arrow (n=4 mice). (**d**) Example lick raster aligned to visual stimulus onset (gray bar) across pre- and post-conditioning, an IP scopolamine session, and a vehicle session. (**e**) Average pre-, post-conditioning, IP scopolamine session lick indices (n=6 mice). (**f**) Baseline lick rates (average from the 5-second period before visual stimulus onset) in pre-conditioning, post-conditioning, and IP scopolamine sessions (n=6 mice). (**g**) Baseline lick rates (average from the 5-second period before visual stimulus onset) in pre-conditioning, post-conditioning, and local scopolamine injection sessions (n=4 mice). (**h**) example pupil images from a representative mouse pre conditioning (top), post conditioning (middle) and following scopolamine (bottom). (**i**) Pupil area from the baseline period in pre- and post-conditioning sessions and local scopolamine injection session (n=4 mice). (**j**) Average pre-, post-conditioning, and scopolamine session lick indices (n=4 mice). (**k**) Traces show visual stimulus-averaged activity before conditioning (n=4 mice) from visual cortex after local injection of either scopolamine or vehicle. For **a**,**b**,**c**,**e**,**f**,**g**,**i**,**j** & **k** data are represented as mean ± SEM.

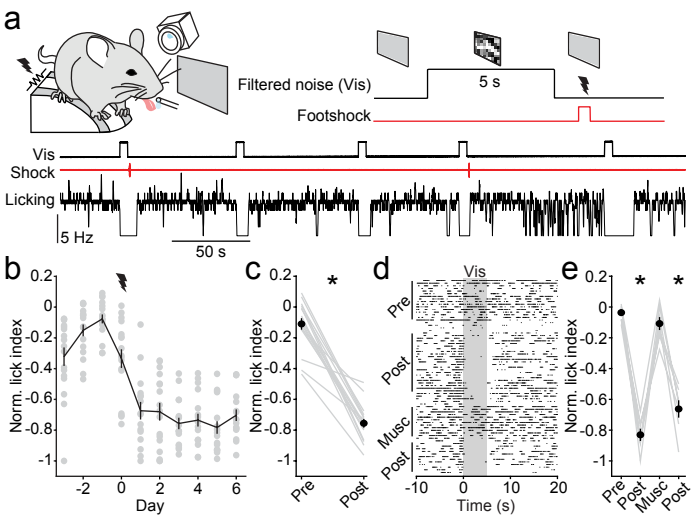

Figure 1

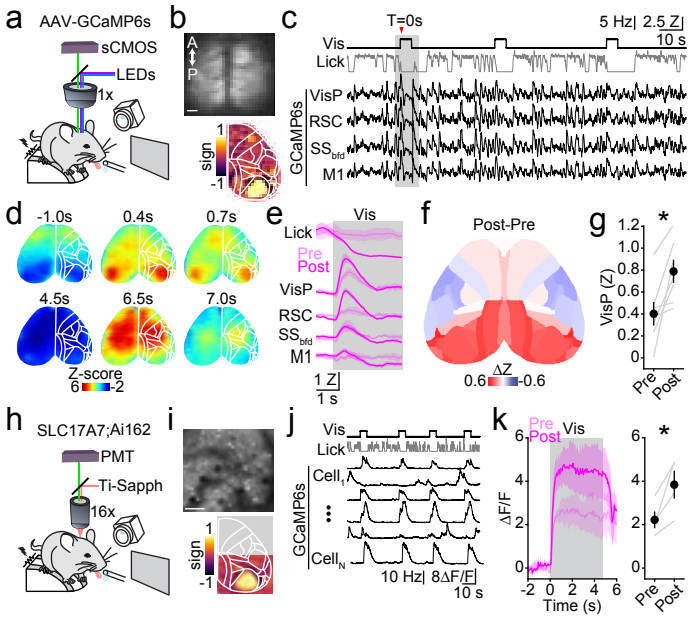

Figure 2

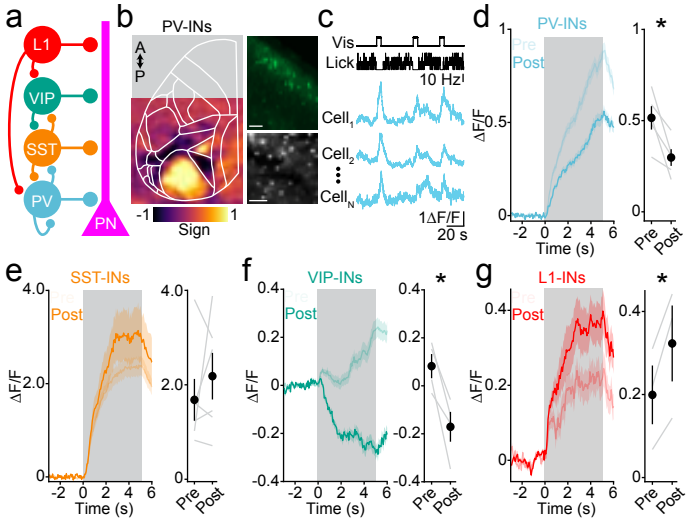

Figure 3

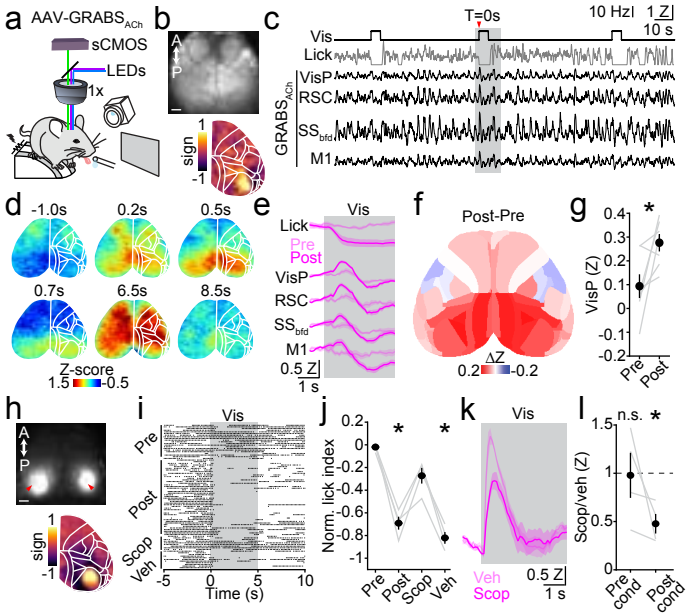

Figure 4

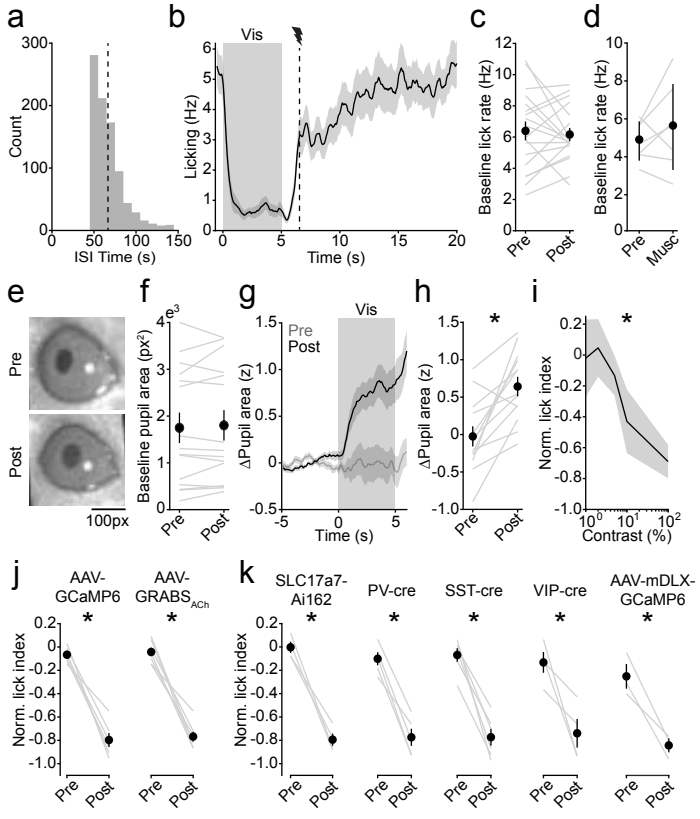

Extended Data Figure 1

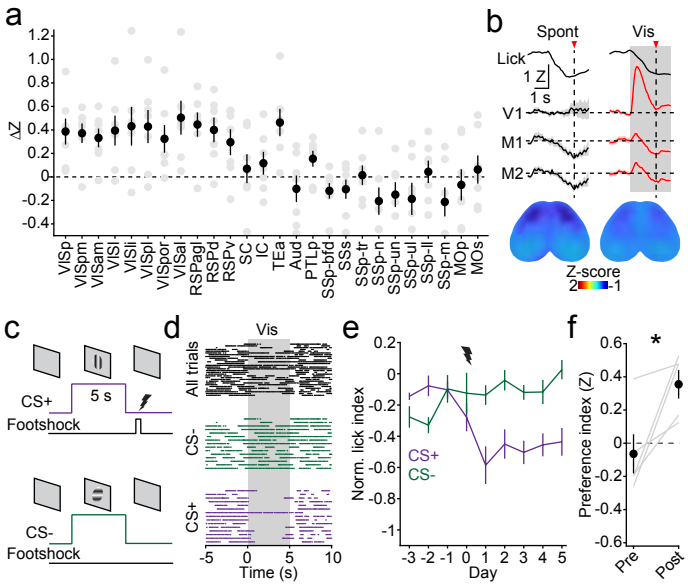

Extended Data Figure 2

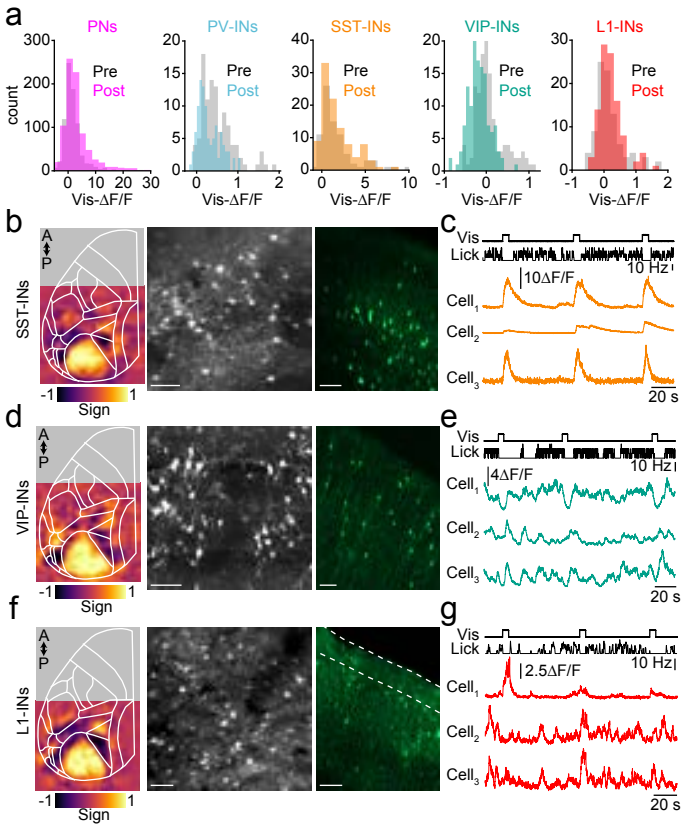

Extended Data Figure 3

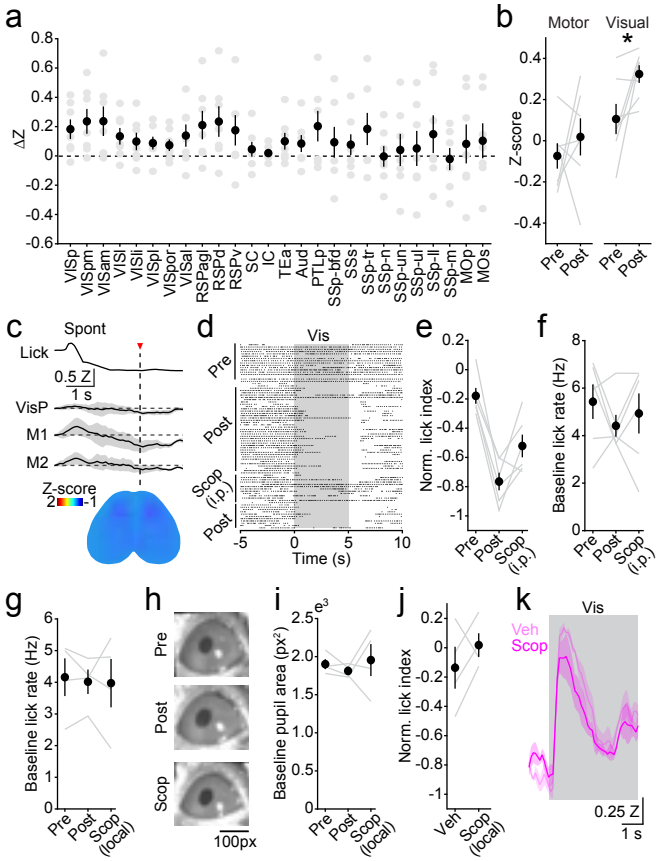

Extended Data Figure 4